Science
AAAS

Supplementary Materials for

A scalable metal-organic framework as a durable physisorbent for carbon dioxide capture

Jian-Bin Lin *et al*.

Corresponding authors: Pierre Hovington, phovington@svanteinc.com; Arvind Rajendran, arvind.rajendran@ualberta.ca; Tom K. Woo, twoo@uottawa.ca; George K. H. Shimizu, gshimizu@ucalgary.ca

Science **374**, 1464 (2021)
DOI: 10.1126/science.abi7281

The PDF file includes:

Materials and Methods

Synthesis of CALF20 single crystals

0.05 g of 2,5-dihydroxy-1,4-benzoquinone was dissolved in 6.0 mL of 50% ethanol. The solution was then added into a solution of 0.18 g of $Zn(NO_3)_2 \cdot 6H_2O$, 0.05 g of 1,2,4-triazole and 6.0 mL of 50% ethanol. The mixture was filtered after stirring for five minutes at room temperature. 6.0 mL of the filtrate was measured and transferred into a 20 mL Teflon autoclave. The autoclave was heated in a convection oven at 180 °C for 48 hours, and then slowly cooled to room temperature in 12 hours before removed from the oven. In situ decomposition to oxalic acid afforded single crystals of CALF20.

Synthesis of CALF20 powder

6.60 g of zinc oxalate, 5.00 g of 1,2,4-triazole and 66.0 mL of methanol were added into a 125 mL Teflon autoclave. The autoclave was heated in a convection oven at 180 oC for 48 hours. The product was washed with 40.0 mL of methanol. 7.30 g of air-dried white powder was collected. The yield is about 70%.

Structuring of CALF20

Powdered CALF20 was structured using a phase inversion method. 0.75 g of polysulfone was added to a beaker containing 6.26 g of N-methyl-2-pyrrolidone and 0.25 g of pluronic F127. The mixture was stirred at room temperature overnight to dissolve polysulfone completely. Then, 9 g of powder CALF20 was added and stirred for 3 hours. The resulting mixture was extruded into a water tank to form a structured CALF20 by solvent/water exchange. The particle density of the structured CALF20 sample was estimated at 570 kg/m3, and the particle size was from 1.0-3.0 mm using polysulfone as a binder. A comparison of powdered and structured CALF20 isotherms is given in Fig. S5.

Single-crystal X-ray diffraction experiment details

Single-crystal X-ray diffraction data was collected at 173(2) K on a Bruker APEX-II CCD diffractometer using Mo Kα radiation ($\lambda = 0.71073$ Å). Crystal was mounted on nylon CryoLoops with Paraton-N. A multi-scan absorption correction was applied to the collected reflections. Using Olex [55], the structure was solved with the ShelXS [58] structure solution program using Direct Methods and refined with the ShelXL [59] refinement package using Least Squares minimisation. All non-hydrogen atoms were refined anisotropically. The organic hydrogen atoms were generated geometrically.

Physical measurements

Powder X-ray diffraction (PXRD) patterns were measured on Bruker D8 Advanced and Rigaku Miniflex II bench top X-Ray diffractometers at room temperature using Cu-Kα radiation ($\lambda = 1.5406$ Å). Thermogravimetric analysis and differential scanning calorimetry (DSC) were recorded on Netzsch STA 409 PC TGA analyser under N2 atmosphere, using an Al pan at a heating rate of 2°C min-1. The FTIR-spectra were recorded on a Nicolet Nexus-470 FT-IR spectrometer using KBr Pellets.

Adsorption Analyses

The adsorption isotherms for CO_2 (99.998%) and N_2 (99.999%) were conducted using an Accelerated Surface Area & Porosimetry System (ASAP) 2020 supplied by Micromeritics Instruments Inc. In a general procedure, the dry sample (~100 mg) was loaded into the glass analysis tube. The sample was heated under vacuum (~10-6 mbar) in two stages, initially to 60 °C at 1°C/min for 2 hrs then to 100 °C at 1°C/min for 12 hrs. After this the outgas rate was less than 2 μbar/hr. The sample was then backfilled with N2 before being transferred to the analysis port where it was evacuated for at least a further 240 min before the analysis was started. Surface areas were calculated using both Langmuir and BET fits. The number of data points in each model were selected to maximize R2, with minimum number of points being 35 for Langmuir and 14 for BET.

Competitive H_2O, CO_2 adsorption measurements

Several papers in the literature measure the loading of CO_2 in the presence of H_2O using a two-step approach. The first step, the regenerated sorbent is saturated with a humid stream, for example Air +H_2O. The mass under these conditions is measured. In step 2 the gas stream is switched to that containing CO_2+H_2O, at the same value of RH as in Step 1. It is not uncommon to assume that the H_2O loadings from step 1 is unaltered in step 2. Hence the difference is mass between steps 1 and 2 is considered as the mass of CO_2 adsorbed. While this can be true in strongly hydrophilic sorbents such as Zeolite 13X, it can lead to inaccurate measurements when dealing with sorbents where CO_2 and H_2O show strong competitive behavior. Hence, it is important to develop experimental methods that avoid this assumption. This means two independent experiments are required. Two approaches can be considered: 1. Perform two experiments each of which can provide the competitive loadings of H_2O and CO_2, respectively. 2. Perform one experiment that provides the total loading of CO_2 and H_2O and a second experiment that provides the competitive loading of either H_2O or CO_2. We adopt the second approach. We use a thermogravimetric analysis to measure the total loading of CO_2 and H_2O, and a dynamic column breakthrough (DCB) experiment to measure the competitive H_2O loading. The difference from the two experiments provides the competitive loadings of CO_2 and H_2O .

Thermogravimetric analysis (TGA)

The total CO_2 and H_2O competitive loadings were measured by a Thermogravimetric analyzer TA Q500 (TA Instruments, DE, USA) from 10% RH to 90% RH at ~295K and 97 kPa total pressure. A bubbler humidifier was used to create streams with varying RH values. This bubbler comprises of a tank filled with deionized water to saturate the feed with water vapour (Fig. S1). A specific RH value can be obtained by controlling the ratio between the dry gas and the humid gas, i.e., by suitably controlling the set points of two mass flow controllers (Alicat Scientific, Tuscon, AZ, USA), MFC-1 and MFC-2. By monitoring the relative humidity meter (RH1, SensorPush, Brooklyn, NY, USA) located at the outlet of the humidifier, a stable RH stream can be generated. In the design available in our laboratory, it took approximately 5-6 hours for the RH value to stabilize. The resulting feed is introduced to the TGA chamber holding ~70 mg of structured CALF20. Since the TGA is gravimetric, only the total mass of the sample and the adsorbates can be measured. Hence, when CO_2 is used as the carrier gas, only the total amount of CO_2 and

H_2O can be measured. The equilibrium is considered to be reached when the change in mass for a period of 120 mins was less than 0.01%. Prior to each experiment, the sample was activated at 423K for 12 hours. This TGA has a weighing precision of ±0.01% and a sensitivity of 0.1µg. The total loading of H_2O and CO_2 measured by the TGA is shown as Curve (1) in fig S15.

Dynamic column breakthrough (DCB)

Dynamic column breakthrough experiments have been used in the literature to measure competitive H_2O- CO_2 loadings [37,60,61] The H_2O loadings from the CO_2+H_2O competitive adsorption were measured by performing adsorption dynamic column breakthrough experiments at different RH values. The dynamic column breakthrough (DCB) apparatus, shown schematically in Fig. S2, was used. The bubbler humidifier was added to the DCB apparatus to generate a humid stream. A 40 mL stainless steel column (Swagelok 304L-HDF2-40, length 7.86 cm; inner diameter 2.82 cm) packed with 16.7 g structured CALF20 was used. Two relative humidity meters (SensorPush, Brooklyn, NY, USA) were placed at the inlet and outlet of the column. The pressure at the inlet and the pressure drop of the column were measured by a pressure transducer and a differential pressure gauge (GE Druck, Billerica, MA, USA). A thermocouple (Omega Engineering, Laval, QC, Canada) was placed 1.82 cm from the column outlet to record the column temperature history. A mass spectrometer (Pfeiffer Vacuum OmniStar GSD 320, Asslar, Germany) was placed at the outlet to record the composition of the effluent gas. All data were recorded every second automatically by a Labview data acquisition system. The column was activated at 423K for 12 hours using helium as a purge gas prior to each experiment. It is important that each experiment is performed long enough that outlet concentrations of both components equal their corresponding inlet values. As seen in Figs 5B and c, each competitive DCB experiment was performed anywhere between $\approx$ 30,000 to 230, 000 s, i.e., 8.3 to 65 hours. At the end of a DCB experiment, the loading of a component i can be calculated by performing a mass balance:

$$n_{i,\,\text{in}} - n_{i,\,\text{out}} = n_{i,acc}$$

Where ni,in and ni,out correspond to the total number of moles at the inlet and outlet of the column, respectively. Ni,acc is the moles of the component accumulated in the column. The term on the left hand side are measured using detectors and flowmeters. The moles accumulated contains two contributions, one from the moles in the fluid phase present in the interstitial voids and those in the adsorbed phase. The moles in the intersitial voids can be calculated based on the measurements of pressure, temperature and knowledge of the void space. Hence, the only unknown quantity is the moles adsorbed. Hence, this quantitiy can be calculated. In this study, the competitive H_2O loading measured from DCB measurements are shown as Curve (2) in Fig. S. Finally, the competitive loading of CO_2 can now be obtained from difference of Curves 1 and 2. This is shown as Curve (3) in Fig. S15.

Cyclic Oxidation Test on TGA

35 mg sample of CALF20 was loaded in Q500 TA TGA instrument connected to dry air as carrier gas and a certified 15%CO_2/85% He gas bottle. The gas flowrate was set

as 200 ml/min for both gases. the sample ramped up under dry air at 10C/min up to 150°C, and then kept for 90 min, and then cooled down to 50 °C under dry air, followed by switching the air to 15% CO_2 gas for CO_2 uptake measurement. This cycle was repeated 30 times and results showed that the CO_2 uptake was unchanged confirming CALF20 material is completely air stable at 150 °C during this total testing period (5000 min or 83 hrs).

Natural gas boiler flue gas exposure of CALF20 Powder

A natural gas boiler generating flue gas and steam is used at the Svante test unit [100 kg CO_2 capture/day demonstration unit]. The flue gas flowrate was controlled by rotameter at 70-100 cc/min. The U-tube chamber was filled with 1g CALF20 powder and wool in order to avoid powder splash, and whole system was heat controlled by mantel at 50°C to avoid any flue gas condensation (Figure S3). The flue gas inlet temperature going through the chamber was 40 °C, and saturated with water vapor. Flue gas composition was measured by GC gas analyzer and presented (Table S4).

Computational Details

Force Field

Grand canonical Monte Carlo (GCMC) simulations were performed such that the framework of the MOF was fixed to that of the experimental crystal structure. Guest molecule – framework interactions were modeled with Lennard-Jones (LJ) potentials to account for the non-bonded steric and dispersion interactions while the fixed partial atomic charge model was used to model non-bonded electrostatic interactions. LJ parameters from the Universal Force Field (UFF)[62], were used for framework atoms. The intermolecular potential parameters for CO_2 guest molecules were obtained from Garcia-Sánchez et al. adsorption in zeolites[63]. The parameters for N_2 guest molecules were taken from the N_2-NIMF parameters developed in-house[64] to reproduce experimental N_2 uptake isotherms in MOFs. TIP4P-Ew[65] parameters were used for the LJ parameters for water. In a comparison of several common water force fields, namely SPC/E, TIP3P, TIP4P, TIP4P/Ew, TIP5P, and TIP5P/Ew, the TIP4P-Ew potential gave the best overall agreement to the experimental water adsorption isotherms in a series of 8 MOFs.[66] Specific parameters used for each atom type can be found in Tables S1 and S2. Lorentz-Berthelot mixing rules were used to determine LJ parameters between atoms of different types. Partial atomic charges on the framework atoms were determined from an electrostatic potential fit to periodic Density Functional Theory (DFT) calculation of CALF20 using the REPEAT method.[67] The DFT calculation was performed using the Vienna Ab initio Simulation Package (VASP)[68-70]. The Perdew–Burke–Ernzerhof (PBE) functional[71] and projector augmented-wave (PAW) pseudopotentials[72] were used with a plane wave energy cut-off of 400 eV. The REPEAT partial atomic charges for CALF20 can be found in Table S3.

Grand Canonical Monte Carlo Simulations

Grand Canonical Monte Carlo (GCMC) simulations were performed using an in-house developed code based on the DL_POLY classic molecular dynamics package[*73*]. GCMC simulations excluding simulations that contained water were run for $12x10^6$ equilibration steps and $32x10^6$ production steps. CO_2/N_2 GCMC separations were carried out isothermally at 293 K with a CO_2:N_2 ratio of 20:80. Adsorption isotherms were calculated for total pressures ranging from 0.01 to 1.2 bar. For the pure water isotherms, a separate GCMC simulation was performed for each relative humidity ranging from 10 to 100% where 100% corresponds to 0.02338 bar which is water's saturation pressure at 293 K. For the adsorption simulations, an empty MOF framework was used as a starting point. Desorption simulations were also performed in order to ensure that equilibrium had been reached for each pressure point. For these desorption simulations, a water-saturated MOF generated using GCMC at 0.1 bar was used as a starting point. The number of equilibration steps was determined by examining the plot of uptake as a function of GCMC steps. Production steps began once the number of adsorbed water molecules showed reasonable stabilization. The simulations were performed by going 'forward and backward' along the range of pressures. The initial configuration and water molecules from a next lower/higher pressure were used as a starting point. For each pressure point, 500 million production steps were performed and the average uptake for the production steps was used as a single data point in the isotherm. Similarly, the isotherms for $CO_2/N_2/H_2O$ gas mixtures were also generated by calculating uptake for each gas component at relative humidity ranging from 10 to 100% where 100% corresponds to 0.02338 bar (water's saturation pressure at 293 K). The total pressure of CO_2 and N_2 was kept at 1 bar with a CO_2:N_2 ratio of 20:80.

Isosteric heat of adsorptions (HOA) were calculated from the GCMC simulations via the Green – Kubo fluctuation theory expression,

$$q_{isosteric} = \frac{\langle UN \rangle - \langle U \rangle \langle N \rangle}{\langle N^2 \rangle - \langle N \rangle \langle N \rangle} + RT$$

where N is the number of guest molecules in the GCMC simulation and U is the total configuration energy for the guest molecules.

Binding Site Analysis

Binding sites were determined from the probability distributions generated from the GCMC simulations using an in-house code as reported in [*13*]. The probability distributions are computed by storing, or binning, the positions of the adsorbed guest atoms at each post-equilibration GCMC step in a 3-dimensional real-space grid. The simulation cell is discretized in each cell vector direction using a grid size of 0.15 Å. The resulting 3D histogram data contains averaged values of the guest atom distributions over the span of a GCMC simulation which, by its construction, samples the free energy of the system. It can be said that maximum values found in the histogram are the regions of highest residence or occupancy of the guest molecules. These maxima correspond to wells in the free energy surface of the system and are thus considered free energy binding sites in the MOF pores. The task of identifying these maxima and assigning binding sites in an automated fashion is briefly described here.

The landscape of the probability distributions can be quite rough due to the statistical noise of the stochastic sampling process even when a large number of MC steps is used. To reduce the sampling noise, several strategies were employed. First, the probability distributions of the supercell cell simulation were folded into that of the single unit cell. Additionally, an equitable binning process was utilized. In normal binning, the position of an atom is assigned to the closest grid point and a value of 1 is inserted into grid-point or "bin". When using equitable binning, the distance to the eight closest grid points are identified and the value of 1.0 is distributed proportionally based on how close the atom is to each grid point and those fractions inserted into the eight individual bins. To further smooth the data, a Gaussian filter was utilized. Other noise reduction filters, such as lowpass filters and median filters were tested, however the Gaussian filter was found to give the best results and is very efficient. Our implementation makes use of the 3D Gaussian filter implemented in SciPy[*74*] which convolutes three1-D Gaussian kernels:

$$G(x,\sigma) = -\frac{1}{\sqrt{2\pi}\sigma} e^{\frac{-x^2}{2\sigma^2}}$$

where σ (sigma) is the standard deviation of the Gaussian kernel. The Gaussian filter is equivalent to a low pass filter with a parabolic attenuation to decrease the high frequency noise but is applied in real space. A σ value of 2.0 Å was used. If more than one maximum is within the 0.675 Å of other maxima, only the maximum with the highest occupancy is retained. Additionally, only maxima greater than 10% of the highest probability found were considered.

Figure S11 shows the most probable binding sites for CO_2 and H_2O in multicomponent simulations. The CO_2 binding site at 20%RH (Figure S11a) is nearly identical to the CO_2 binding site (Figure 3a of main text) from the binary CO_2/N_2 simulation and has a binding energy of -33.5 kJ/mol. However, at 60%RH, when CO_2 has been outcompeted by water, there is a notable change in the CO_2 binding site, where the internuclear axis is now in the *bc* plane instead of along the *a*-axis (Figure S11c). Furthermore, the CO_2 binding site has oriented toward the triazole linkers. Interestingly, the binding site at 60% RH is 2 kJ/mol stronger than that from the 20% RH simulation (Table S6). For water, the binding sites remain essentially the same, where the sites are located at the four corners of each pore, and the most probable binding site is oriented away from the framework to maximize H-bonding interactions with other water guest molecules (Figures S11b, S11d). As seen with CO_2, minor changes in the binding site of water in these simulations results in a decrease in binding energy by ~2 kJ/mol from 20% RH to 60% RH, with guest-guest interactions becoming more important for increased loading at higher RH (Table S6). This effect is further supported by the drastic increase in the heat of adsorption (HOA) for water from 1% RH to 100% RH compared to the minute change in the HOA for CO_2 (Table S7).

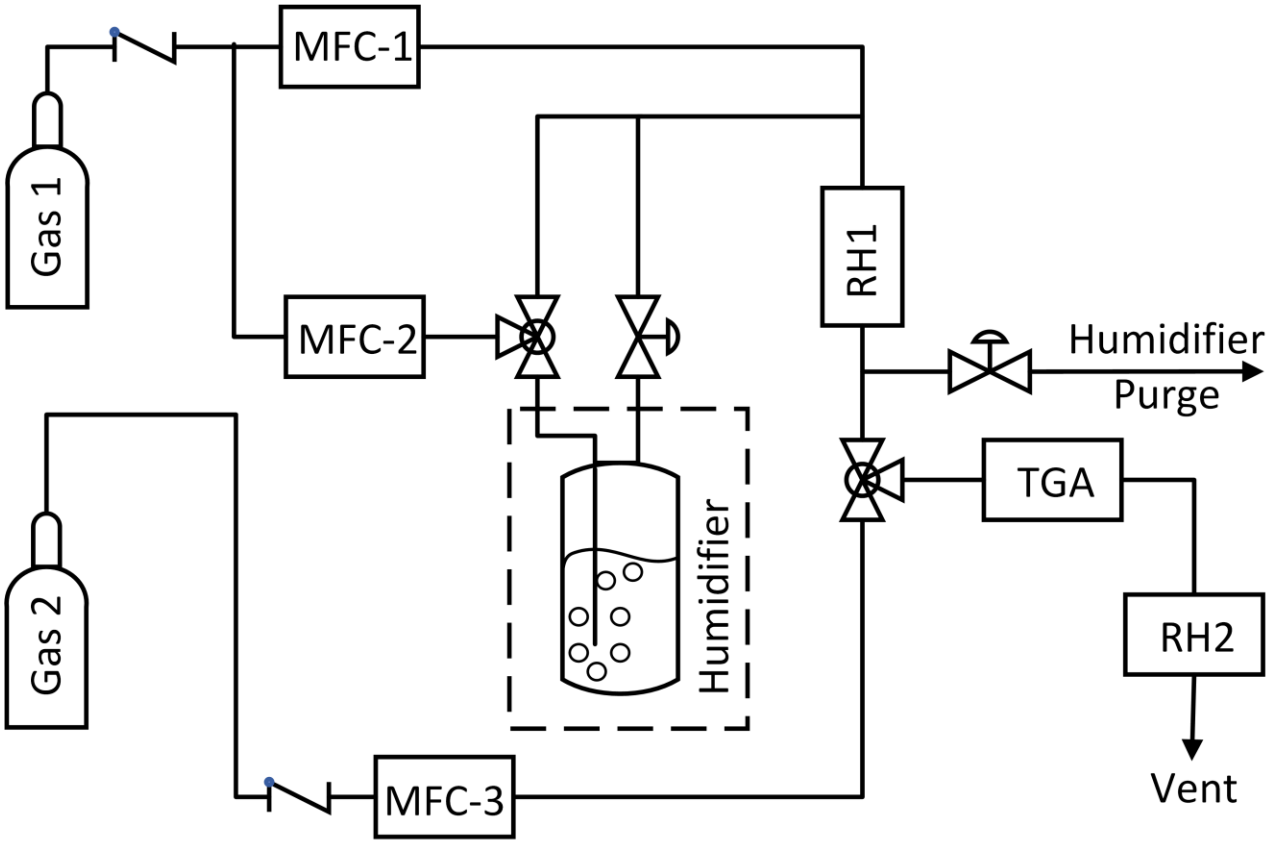

Fig. S1

The schematic of the thermogravimetric analyzer coupled with the bubbler humidifier. MFC: Mass flow controller; RH: Relative humidity meter; TGA: Thermogravimetric analyzer.

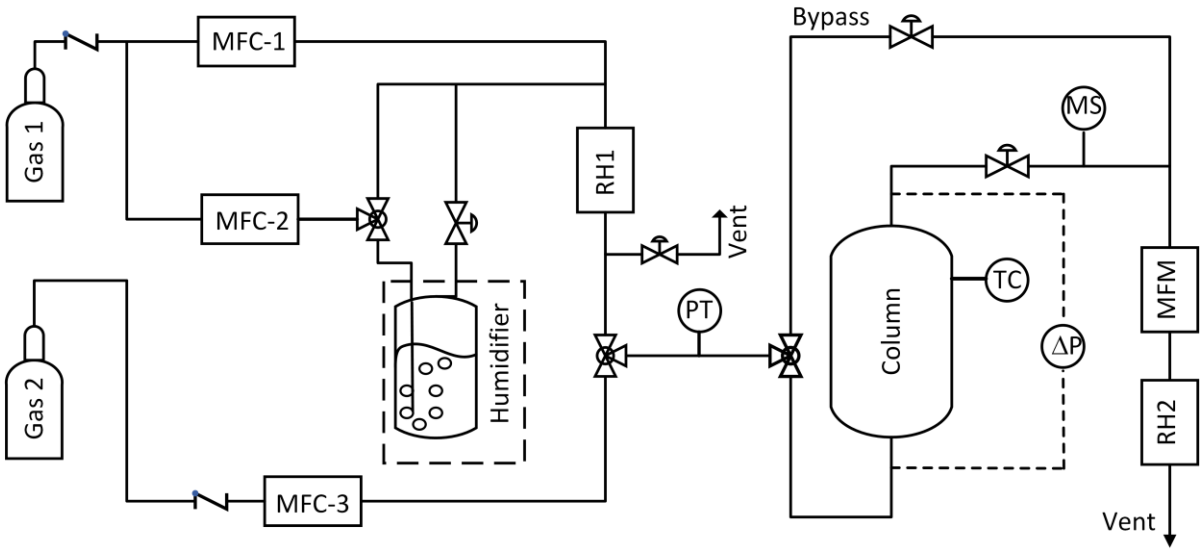

Fig. S2

The CO_2+H_2O dynamic column breakthrough apparatus. MFC: Mass flow controller; RH: Relative humidity meter; MS: Mass spectrometer; PT: Pressure transducer; TC: Thermocouple; MFM: Mass flow meter.

Fig. S3
Test rig for flue gas exposure of CALF20 from a natural gas burner.

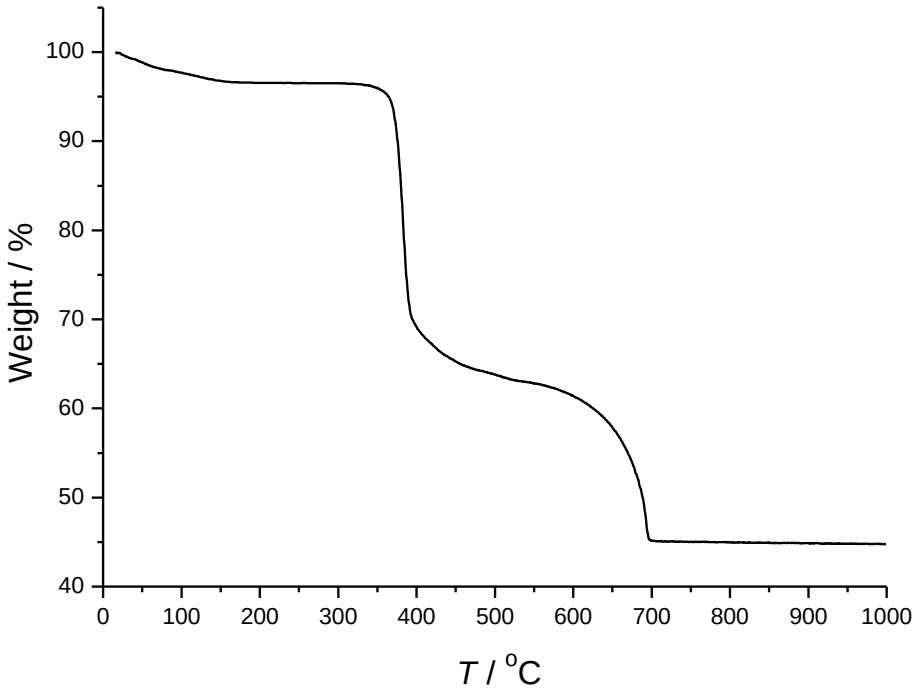

Fig. S4
TGA of CALF20 under air atmosphere.

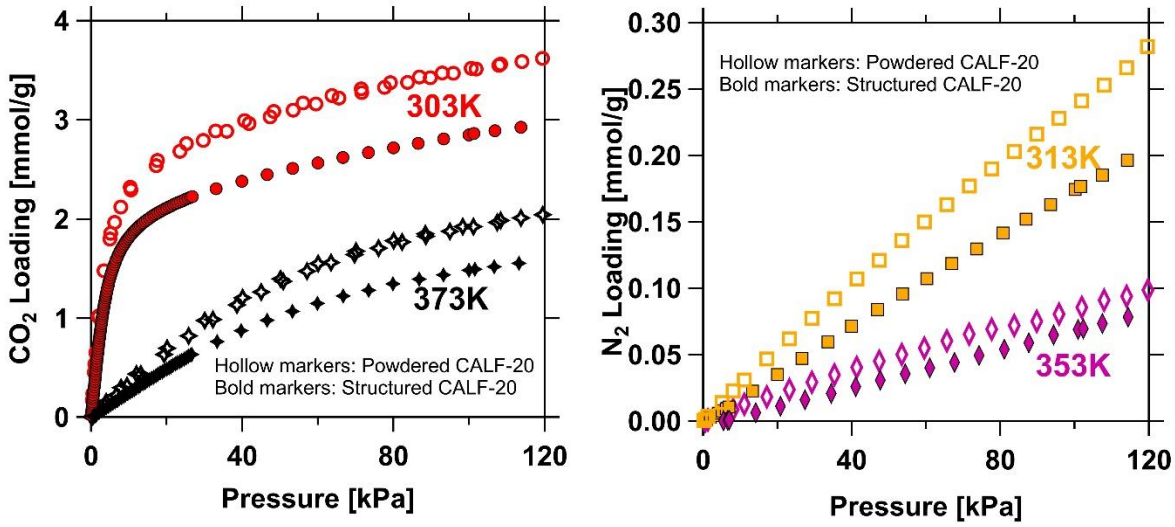

Fig. S5

Comparison of CO_2 and N_2 isotherms of pure and structured CALF20 at different temperatures. Hollow markers are the isotherms of powdered CALF20; Bold (filled) markers are the isotherms of structured CALF20.

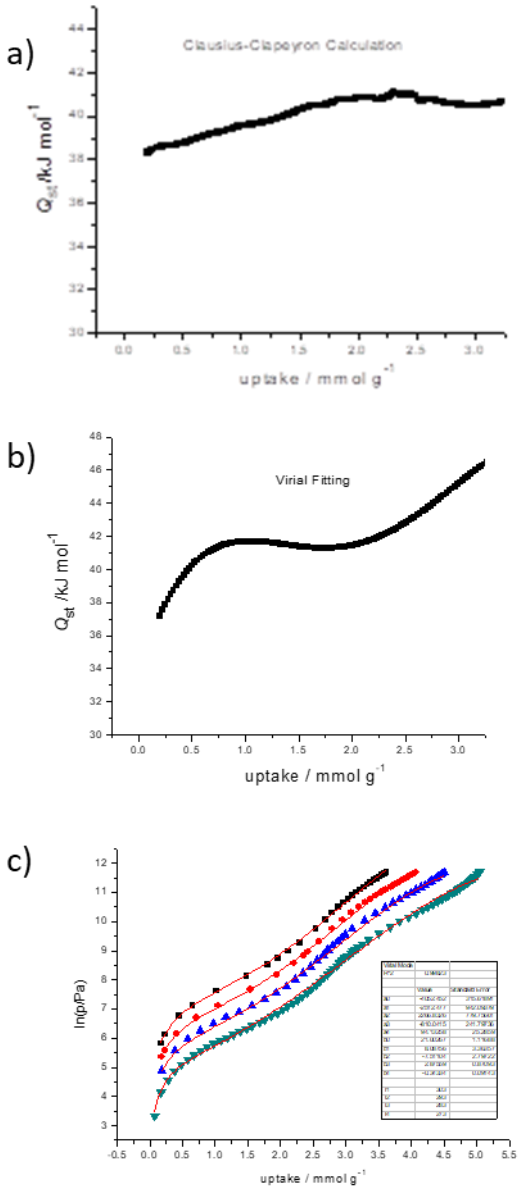

Fig. S6
Qst values calculated using (a) the Clausius-Clapeyron equation and (b) virial model with the isotherms at 273, 283, 293, and 303 K. (c) The fitting parameters of the virial model with the isotherms at 273, 283, 293, and 303 K.

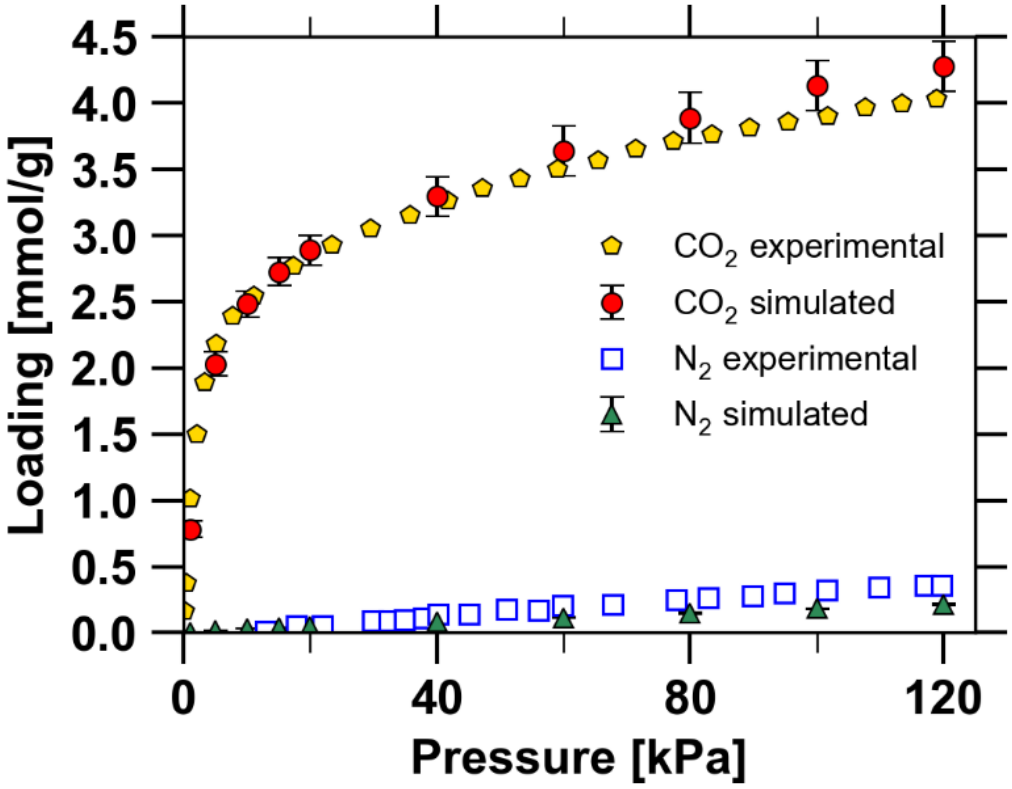

Fig. S7

Computed and experimental CO_2 and N_2 single component isotherms at 293 K.

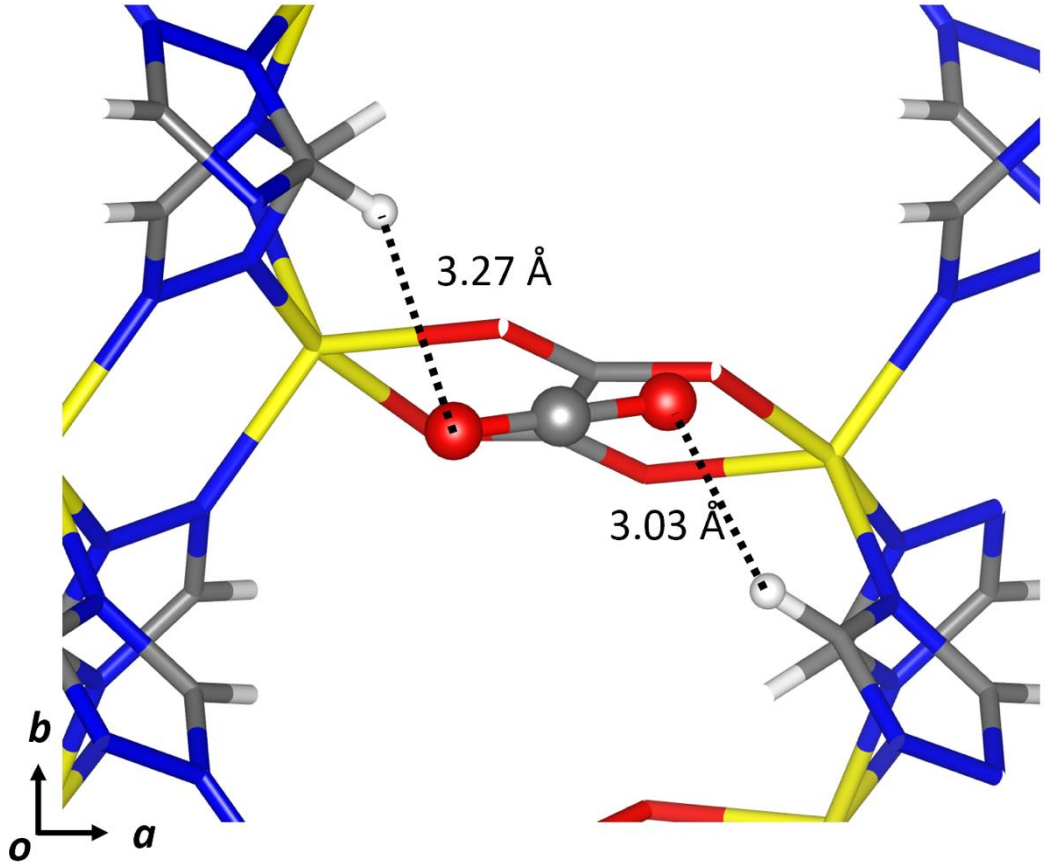

Fig. S8

The two shortest interatomic distances between CO_2 and the CALF20 framework in the most probable CO_2 binding site extracted from a water-free binary GCMC simulation of 0.2 bar CO_2, 0.8 bar N_2 and 293 K.

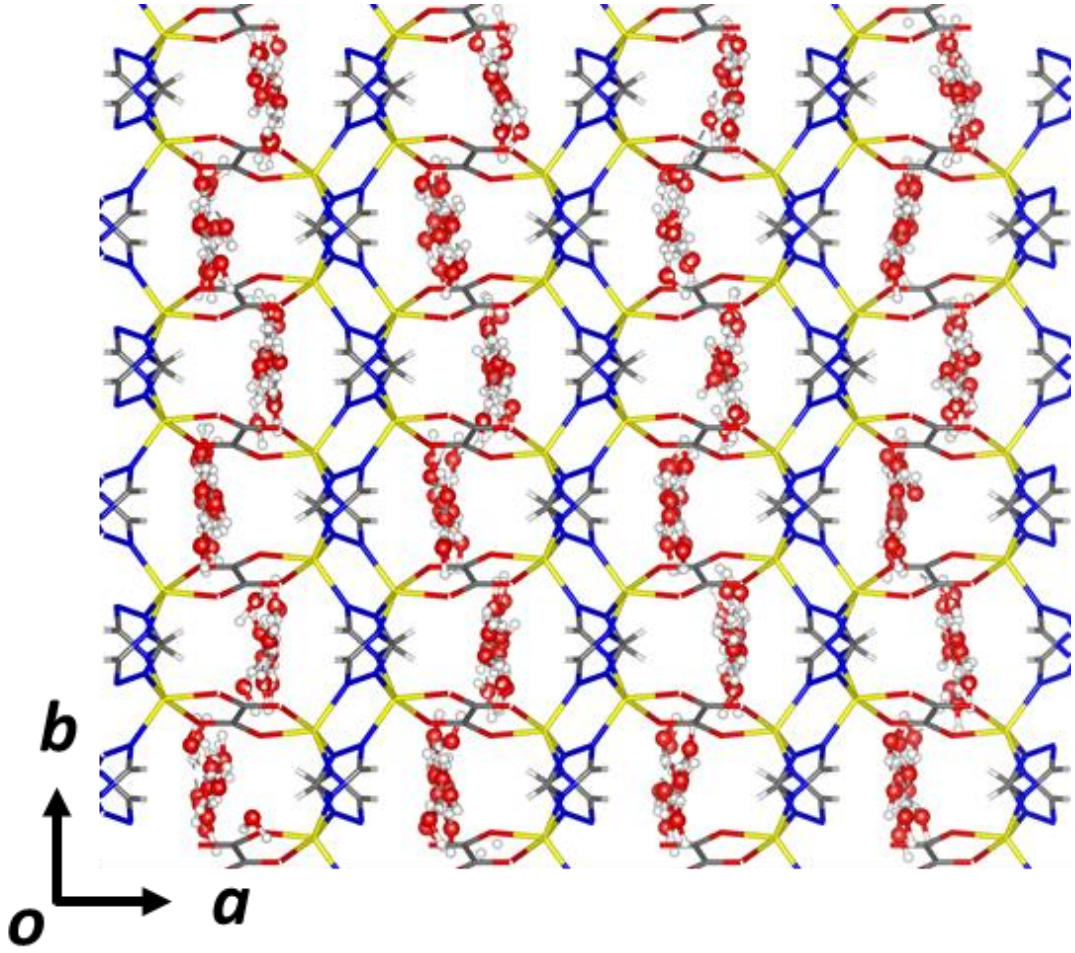

Fig. S9

A single configuration from a GCMC simulation (following equilibration) of water at 60% RH at 293 K.

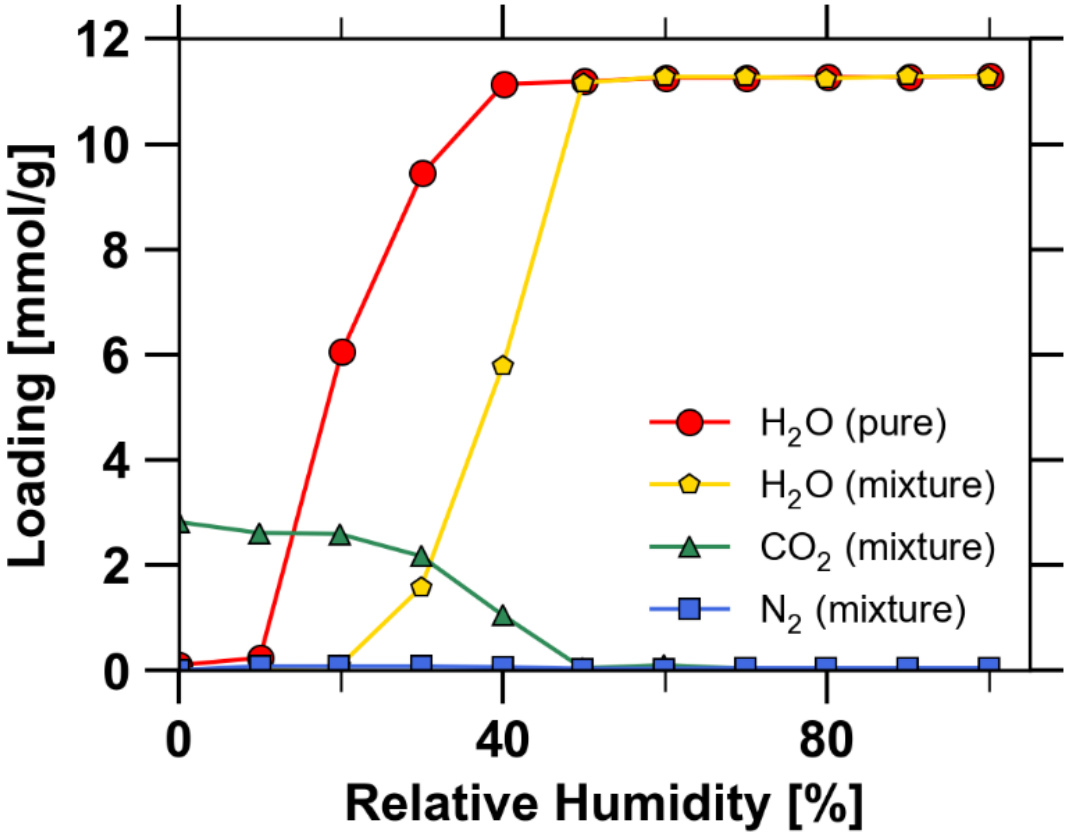

Fig. S10

Guest loadings from GCMC simulations at different relative humidities from single component water simulations and multicomponent CO_2/N_2/water simulations at 293 K. CO_2 and N_2 were at 0.2 and 0.8 atm, respectively in the multi-component simulations.

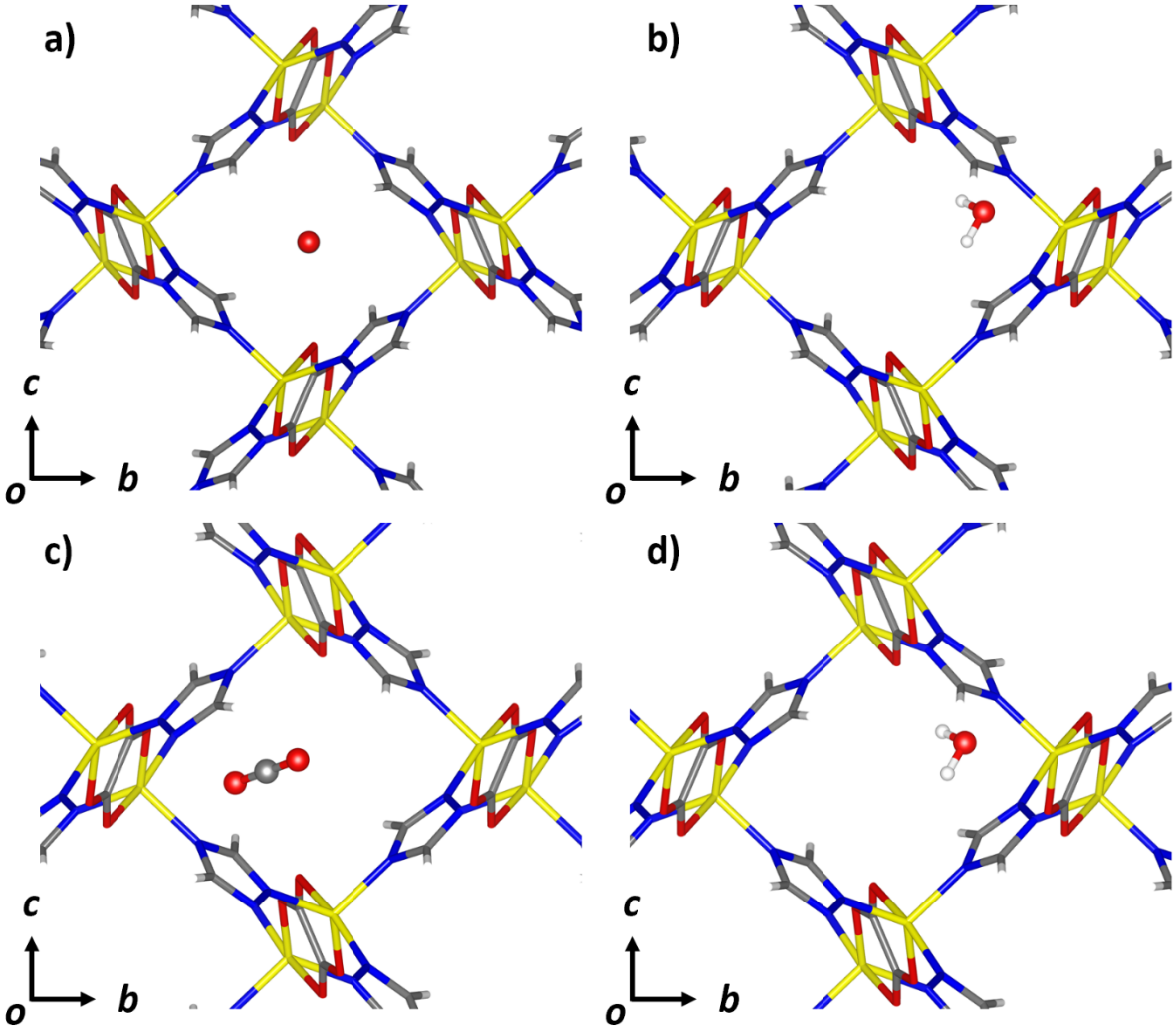

Fig. S11

Most probable a), d) CO_2 and b), d) H_2O binding sites from multicomponent $CO_2/N_2/H_2O$ simulations (293 K; 1 bar total pressure; CO_2:N_2 20:80; RH: a), b) 20%, c), d) 60%.

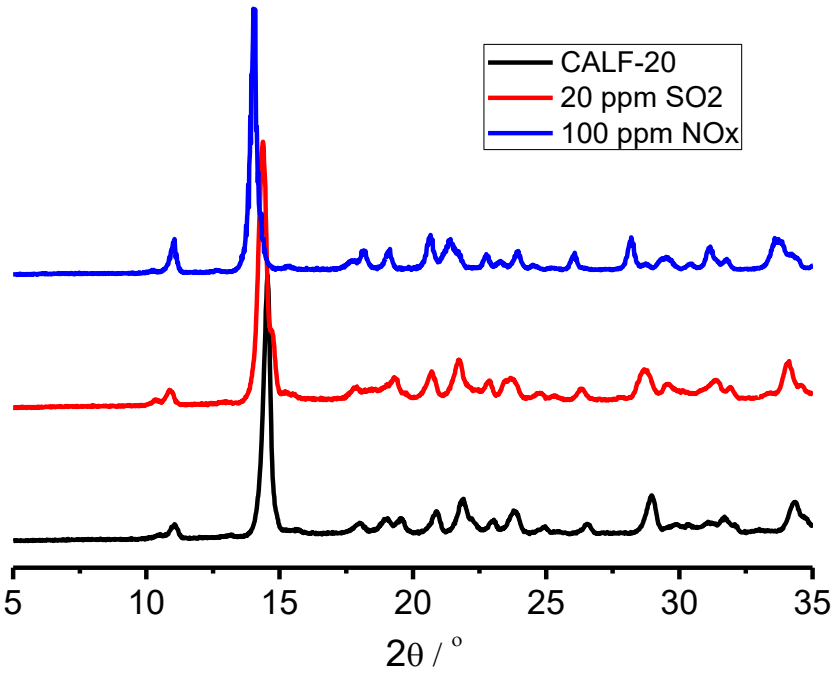

Fig. S12

PXRD of pristine CALF20 and after three hours exposure to acid gases as listed.

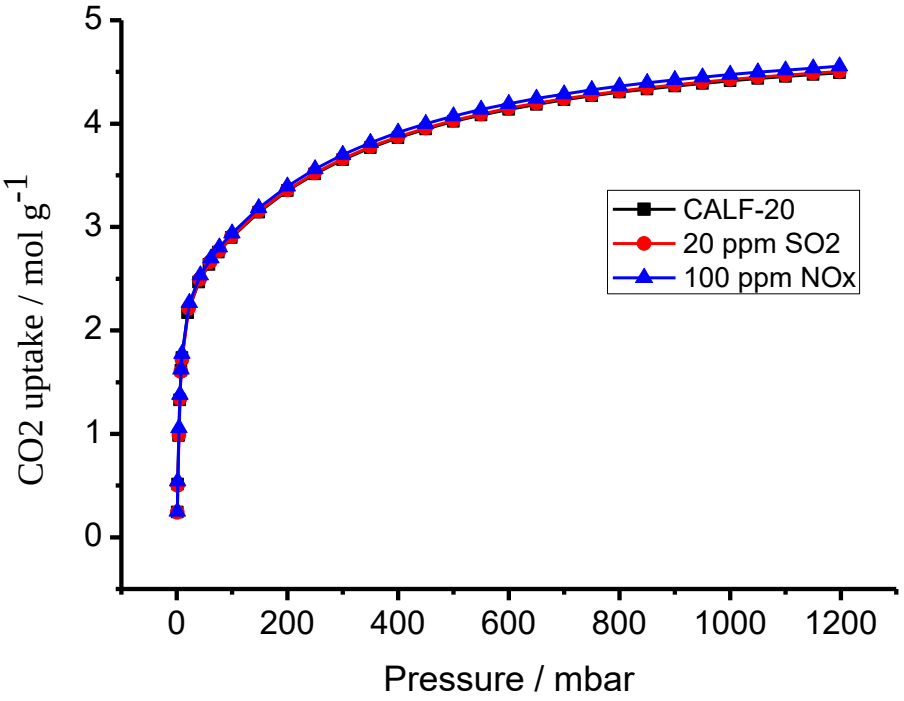

Fig. S13

CO_2 isotherm (273 K) of CALF20 pristine and after three hours exposure to acid gases as listed.

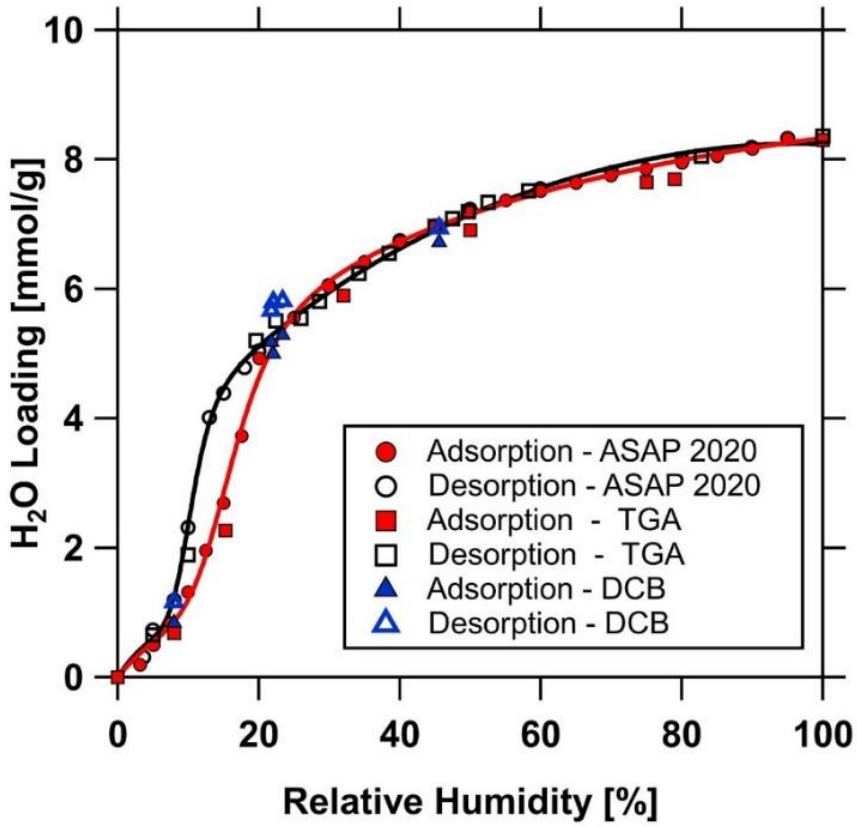

Fig. S14

Comparison of H_2O loading at 22 °C measured by a volumetric apparatus (ASAP 2020), thermogravimetric analyzer (TGA) and dynamic column breakthrough (DCB) experiments. The plot shows excellent match between three independent experimental techniques confirming the suitability of DCB experiments for measurement of adsorption equilibria.

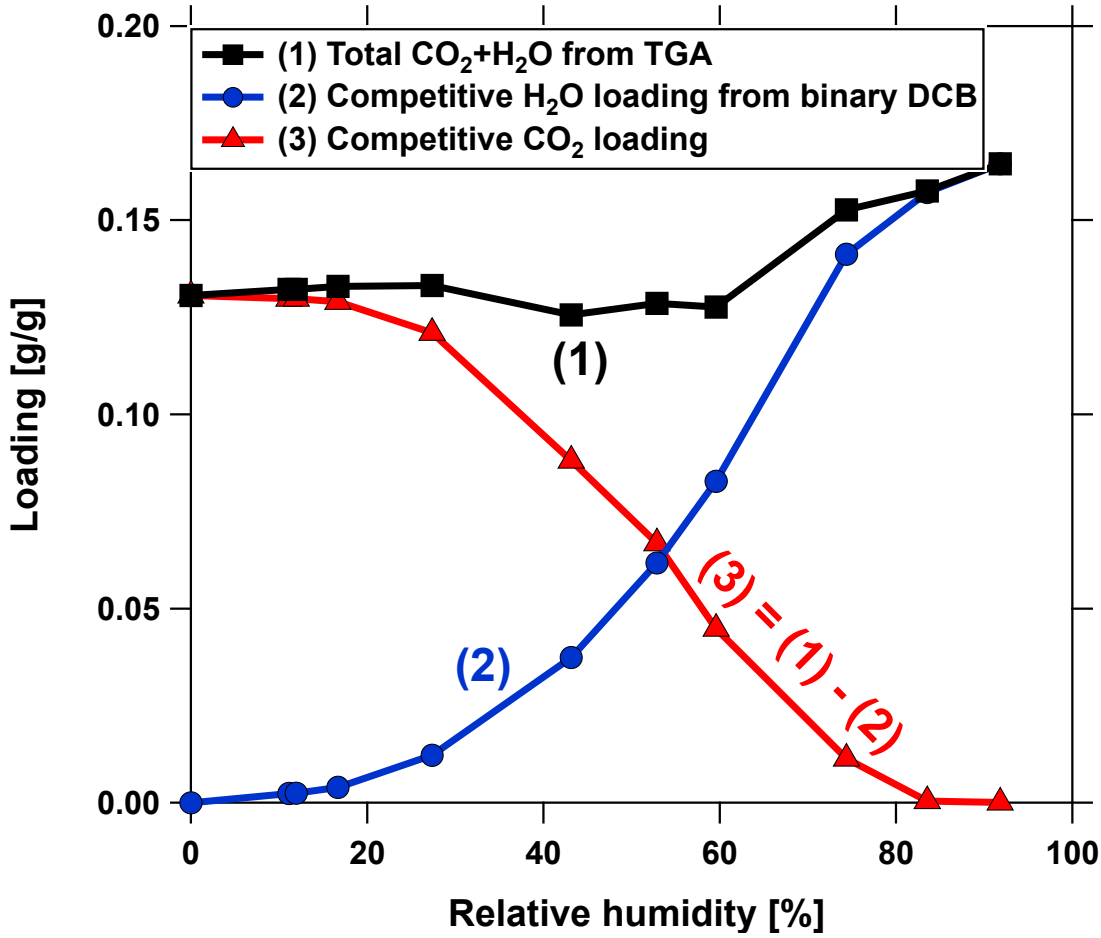

Fig. S15

Measurement of competitive H_2O+CO_2 loadings at 97 kPa bar and 295 K. Curve (1) is the total CO_2+H_2O loading measured using a thermogravimetric analyzer in a dynamic mode by passing CO_2 saturated with various values of RH. Curve (2) is the competitive loading of H_2O measured by performing a mass balance for H_2O in binary dynamic column breakthrough experiment involving mixtures of CO_2 and H_2O. Curve (3) is the difference between curves (1) and (2) providing the competitive CO_2 loading.

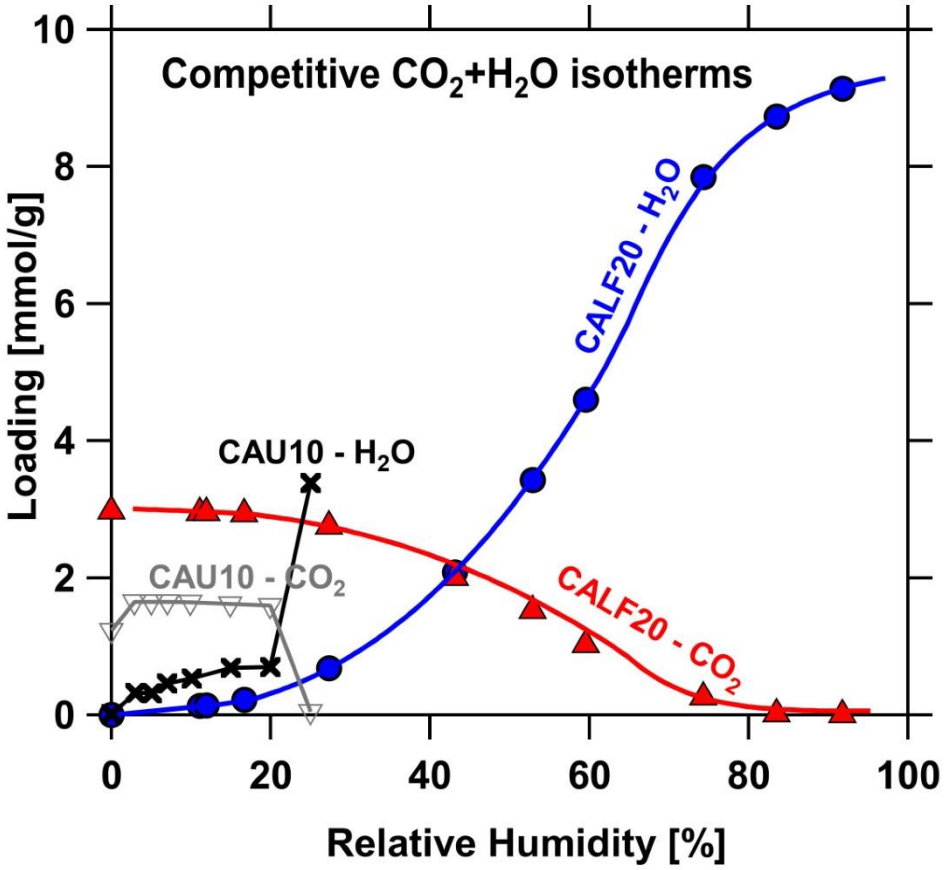

Fig. S16

Comparison of competitive CO_2 and H_2O isotherms (295 K) of CALF20 and CAU-10 (*38*) as a representative hydrophobic MOF.

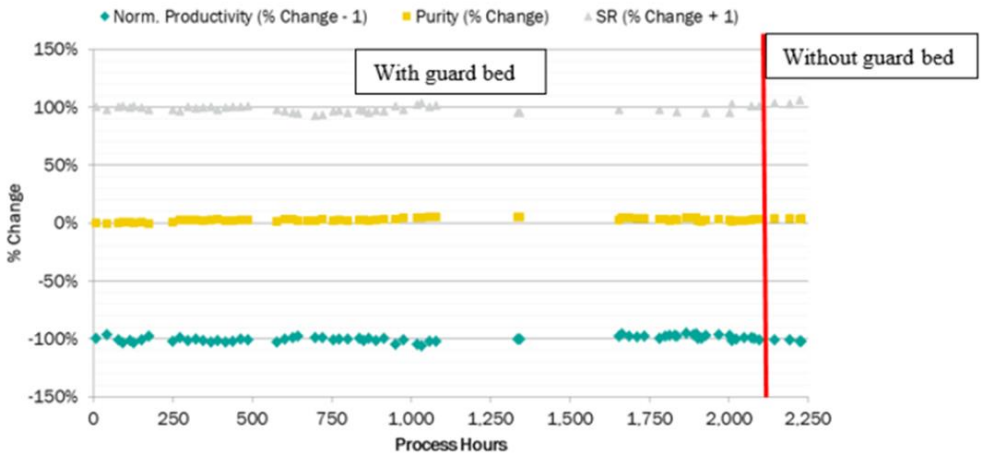

Fig. S17

Changes in KPIs (productivity, purity of recovered CO_2 and steam ratio (SR) needed) over >2000 hours of operation in a CALF20 demonstration unit that included a preliminary particulate and SOx scrubbing . The guard bed refers to an activated carbon to reduce NOx. Notably, performance is retained for over 200 hours testing when the NOx guard is removed. Details in ref. 48.

Table S1.
Universal force field (UFF) parameters for framework atoms used in GCMC simulations.

CALF20 Framework		
Atom	**ε (kcal/mol)**	**σ (Å)**
Zn	0.124	2.4616
N	0.069	3.2607
O	0.06	3.1181
C	0.105	3.4309
H	0.044	2.5711

Table S2.

Force field parameters and charges for guest molecules used in GCMC simulations.

H_2O			
Atom	**ε (kcal/mol)**	**σ (Å)**	**Charge**
O_w	0.16275	3.16435	0
H_w	0	0	0.52422
H_w	0	0	0.52422
H_x	0	0	-1.04844
CO_2			
Atom	**ε (kcal/mol)**	**σ (Å)**	**Charge**
C	0.05948	2.745	0.6512
O	0.17023	3.017	-0.3256
O	0.17023	3.017	-0.3256
N_2			
Atom	**ε (kcal/mol)**	**σ (Å)**	**Charge**
N	0.07942	2.45491	-0.482
N	0.07942	2.45491	-0.482
COM	0	0	0.964

Table S3.

CALF20 REPEAT atomic charges and fractional atomic coordinates.

Atom	x	y	Z	Charge	Atom	x	y	z	Charge
Zn	0.1759	0.0577	0.4368	0.68714	**O**	0.3247	0.9693	0.3268	-0.51882
Zn	0.8241	0.5577	0.0632	0.68715	**O**	0.6753	0.4693	0.1732	-0.51882
Zn	0.8241	0.9423	0.5632	0.68715	**C**	0.0215	0.8017	0.2588	0.19037
Zn	0.1759	0.4423	0.9368	0.68714	**C**	0.9785	0.3017	0.2412	0.19040
N	0.0308	0.8892	0.368	-0.27848	**C**	0.9785	0.1983	0.7412	0.19040
N	0.9692	0.3892	0.1317	-0.27851	**C**	0.0215	0.6983	0.7588	0.19037
N	0.9692	0.1108	0.6317	-0.27851	**H**	0.0932	0.8045	0.2086	0.09334
N	0.0308	0.6108	0.8683	-0.27847	**H**	0.9068	0.3045	0.2914	0.09333
N	0.9078	0.8525	0.4100	-0.10487	**H**	0.9068	0.1955	0.7914	0.09333
N	0.0922	0.3525	0.0900	-0.10483	**H**	0.0932	0.6955	0.7086	0.09334
N	0.0922	0.1475	0.5900	-0.10483	**C**	0.8345	0.7446	0.3232	0.16283
N	0.9078	0.6475	0.9100	-0.10487	**C**	0.1655	0.2446	0.1768	0.16281
N	0.9008	0.7086	0.2259	-0.33557	**C**	0.1655	0.2554	0.6768	0.16282
N	0.0992	0.2086	0.2741	-0.33557	**C**	0.8345	0.7554	0.8232	0.16283
N	0.0992	0.2914	0.7741	-0.33558	**H**	0.7441	0.6971	0.3289	0.11265
N	0.9008	0.7914	0.7259	-0.33556	**H**	0.2559	0.1971	0.1711	0.11266
O	0.4098	0.0761	0.6102	-0.55677	**H**	0.2559	0.3029	0.6711	0.11266
O	0.5902	0.5761	0.8898	-0.55675	**H**	0.7441	0.8029	0.8289	0.11265
O	0.5902	0.9239	0.3898	-0.55675	**C**	0.5248	0.0308	0.5815	0.54816
O	0.4098	0.4239	0.1102	-0.55677	**C**	0.4752	0.5308	0.9185	0.54813
O	0.6753	0.0307	0.6732	-0.51882	**C**	0.4752	0.9692	0.4185	0.54814
O	0.3247	0.5307	0.8268	-0.51881	**C**	0.5248	0.4692	0.0815	0.54817

Table S4.

Natural gas boiler flue gas composition for durability testing of CALF20.

Flue gas composition	**v/v %**
CO_2	**8.6%**
O_2	**7.1%**
H_2O	**7.3%**
NO	**78 ppm**
NO_2	**13.4 ppm**
CO	**147 ppm**
N_2	**Balance**

Table S5.

Crystal data and structure refinement for CALF20.

Identification code	CALF20
Empirical formula	$C_3H_2N_3O_2Zn \cdot 0.396(C_2H_6O)$
Formula weight	195.68
Temperature/K	173(2)
Crystal system	monoclinic
Space group	$P2_1/c$
a/Å	8.9138(12)
b/Å	9.6935(12)
c/Å	9.4836(13)
β/°	115.895(4)
Volume/Å^3	737.17(17)
Z	4
ρ_{calc}g/cm^3	1.763
μ/mm^{-1}	3.279
F(000)	389.0
Crystal size/mm^3	0.15 × 0.10 × 0.06
Radiation	Mo $K\alpha$ (λ = 0.71073)
2θ range for data collection/°	6.362 to 72.82
Index ranges	$-14 \leq h \leq 14$, $-16 \leq k \leq 16$, $-15 \leq l \leq 14$
Reflections collected	19529
Independent reflections	3577 [R_{int} = 0.0614, R_{sigma} = 0.0460]
Data/restraints/parameters	3577/6/105
Goodness-of-fit on F^2	0.993
Final R indexes [I>=2σ (I)]	R_1 = 0.0313, wR_2 = 0.0693
Final R indexes [all data]	R_1 = 0.0550, wR_2 = 0.0769
Largest diff. peak/hole / e Å^{-3}	0.65/-0.49

Table S6.

Calculated binding energies of most probable CO_2 and H_2O binding sites taken from the multicomponent $CO_2/N_2/H_2O$ simulations (CO_2:N_2 = 20:80) at 293 K, 1 bar total pressure, and 20% and 60% RH. The gas uptake at each condition is shown to demonstrate the competitive adsorption effect.

Species (conditions)	**Binding Energy (kJ/mol)**	**vdW component (kJ/mol)**	**Electrostatic component (kJ/mol)**	**Percent electrostatic (%)**	**Gas Uptake (mmol/g)**
CO_2 (20% RH)	-33.5	-28.9	-4.6	13.9	2.59
H_2O (20% RH)	-17.7	-9.0	-8.7	49.1	0.08
CO_2 (60% RH)	-35.8	-26.6	-9.1	25.6	0.10
H_2O (60% RH)	-15.3	-7.8	-7.5	48.9	11.28

Table S7.

Heats of adsorption of CO_2 and H_2O at 0.1 bar CO_2/1% RH and 1.0 bar CO_2/100% RH, determined from GCMC simulations. $\Delta(\Delta H_{ads})$ represents the change in the heat of adsorption from low pressure conditions to high pressure conditions.

Species	ΔH_{ads} (kJ/mol) 0.1 bar CO_2, 1% RH	ΔH_{ads} (kJ/mol) 1.0 bar CO_2, 100% RH	$\Delta(\Delta H_{ads})$ (kJ/mol)
CO_2	-40[a]	-42	-2
H_2O	-36	-64	-28

[a]the experimental zero-loading HOA of CO_2 was determined to be 39 kJ/mol.

References and Notes

1. "Accelerating Breakthrough Innovation in Carbon Capture, Utilization, and Storage" (U.S. Department of Energy, 2017).

2. Z. Hu, Y. Wang, B. B. Shah, D. Zhao, Capture in metal-organic framework adsorbents: An engineering perspectiv. *Adv. Sustainable Syst.* **3**, 1800080 (2018). doi:10.1002/adsu.201800080

3. K. Sumida, D. L. Rogow, J. A. Mason, T. M. McDonald, E. D. Bloch, Z. R. Herm, T. H. Bae, J. R. Long, Carbon dioxide capture in metal-organic frameworks. *Chem. Rev.* **112**, 724–781 (2012). doi:10.1021/cr2003272 Medline

4. B. Dutcher, M. Fan, A. G. Russell, Amine-based CO_2 capture technology development from the beginning of 2013-a review. *ACS Appl. Mater. Interfaces* **7**, 2137–2148 (2015). doi:10.1021/am507465f Medline

5. M. Wang, A. S. Joel, C. Ramshaw, D. Eimer, N. M. Musa, Process intensification for post-combustion CO_2 capture with chemical absorption: A critical review. *Appl. Energy* **158**, 275–291 (2015). doi:10.1016/j.apenergy.2015.08.083

6. C. Gouedard, D. Picqa, F. Launay, P.-L. Carrette, Amine degradation in CO_2 capture. I. A review. *Int. J. Greenh. Gas Control* **10**, 244–270 (2012). doi:10.1016/j.ijggc.2012.06.015

7. M. Pardakhti, T. Jafari, Z. Tobin, B. Dutta, E. Moharreri, N. S. Shemshaki, S. Suib, R. Srivastava, Trends in solid adsorbent materials development for CO_2 capture. *ACS Appl. Mater. Interfaces* **11**, 34533–34559 (2019). doi:10.1021/acsami.9b08487 Medline

8. L. A. Darunte, K. S. Walton, D. S. Sholl, C. W. Jones, CO_2 capture via adsorption in amine-functionalized sorbents. *Curr. Opin. Chem. Eng.* **12**, 82–90 (2016). doi:10.1016/j.coche.2016.03.002

9. C. A. Trickett, A. Helal, B. A. Al-Maythalony, Z. H. Yamani, K. E. Cordova, O. M. Yaghi, The chemistry of metal-organic frameworks for CO_2 capture, regeneration and conversion. *Nat. Rev. Mater.* **2**, 17045 (2017). doi:10.1038/natrevmats.2017.45

10. A. E. Creamer, B. Gao, Carbon-based adsorbents for postcombustion CO_2 capture: A critical review. *Environ. Sci. Technol.* **50**, 7276–7289 (2016). doi:10.1021/acs.est.6b00627 Medline

11. J. C. Abanades, B. Arias, A. Lyngfelt, T. Mattisson, D. E. Wiley, H. Li, M. T. Ho, E. Mangano, S. Brandani, Emerging CO_2 capture systems. *Int. J. Greenh. Gas Control* **40**, 126–166 (2015). doi:10.1016/j.ijggc.2015.04.018

12. D. G. Madden, H. S. Scott, A. Kumar, K. J. Chen, R. Sanii, A. Bajpai, M. Lusi, T. Curtin, J. J. Perry, M. J. Zaworotko, Flue-gas and direct-air capture of CO_2 by porous metal-organic materials. *Philos. Trans. A, Math. Phys. Eng. Sci.* **375**, 20160025 (2017). doi:10.1098/rsta.2016.0025 Medline

13. P. G. Boyd, A. Chidambaram, E. García-Díez, C. P. Ireland, T. D. Daff, R. Bounds, A. Gładysiak, P. Schouwink, S. M. Moosavi, M. M. Maroto-Valer, J. A. Reimer, J. A. R. Navarro, T. K. Woo, S. Garcia, K. C. Stylianou, B. Smit, Data-driven design of metal-

organic frameworks for wet flue gas CO_2 capture. *Nature* **576**, 253–256 (2019). doi:10.1038/s41586-019-1798-7 Medline

14. E. González-Zamora, I. A. Ibarra, E., Gonzalez-Zamora, I. A. Ibarra, CO_2 capture under humid conditions in metal–organic frameworks. *Mater. Chem. Front.* **1**, 1471–1484 (2017). doi:10.1039/C6QM00301J

15. J. H. Cavka, S. Jakobsen, U. Olsbye, N. Guillou, C. Lamberti, S. Bordiga, K. P. Lillerud, A new zirconium inorganic building brick forming metal organic frameworks with exceptional stability. *J. Am. Chem. Soc.* **130**, 13850–13851 (2008). doi:10.1021/ja8057953 Medline

16. A. J. Howarth, Y. Liu, P. Li, Z. Li, T. C. Wang, J. T. Hupp, O. K. Farha, Chemical, thermal and mechanical stabilities of metal-organic frameworks. *Nat. Rev. Mater.* **1**, 15018 (2016). doi:10.1038/natrevmats.2015.18

17. J. M. Kolle, M. Fayaz, A. Sayari, Understanding the Effect of Water on CO_2 Adsorption. *Chem. Rev.* **121**, 7280–7345 (2021). doi:10.1021/acs.chemrev.0c00762 Medline

18. S. Yuan, L. Feng, K. Wang, J. Pang, M. Bosch, C. Lollar, Y. Sun, J. Qin, X. Yang, P. Zhang, Q. Wang, L. Zou, Y. Zhang, L. Zhang, Y. Fang, J. Li, H. C. Zhou, Stable metal-organic frameworks: Design, synthesis, and applications. *Adv. Mater.* **30**, e1704303 (2018). doi:10.1002/adma.201704303 Medline

19. J. Duan, W. Jin, S. Kitagawa, Water-resistant porous coordination polymers for gas separation. *Coord. Chem. Rev.* **332**, 48–74 (2017). doi:10.1016/j.ccr.2016.11.004

20. E. J. Kim, R. L. Siegelman, H. Z. H. Jiang, A. C. Forse, J. H. Lee, J. D. Martell, P. J. Milner, J. M. Falkowski, J. B. Neaton, J. A. Reimer, S. C. Weston, J. R. Long, Cooperative carbon capture and steam regeneration with tetraamine-appended metal-organic frameworks. *Science* **369**, 392–396 (2020). doi:10.1126/science.abb3976 Medline

21. D. F. Sava Gallis, D. J. Vogel, G. A. Vincent, J. M. Rimsza, T. M. Nenoff, NOx adsorption and optical detection in rare earth metal-organic frameworks. *ACS Appl. Mater. Interfaces* **11**, 43270–43277 (2019). doi:10.1021/acsami.9b16470 Medline

22. S. Bhattacharyya, R. Han, W. G. Kim, Y. Chiang, K. C. Jayachandrababu, J. T. Hungerford, M. R. Dutzer, C. Ma, K. S. Walton, D. S. Sholl, S. Nair, Acid gas stability of zeolitic imidazolate frameworks: Generalized kinetic and thermodynamic characteristics. *Chem. Mater.* **30**, 4089–4101 (2018). doi:10.1021/acs.chemmater.8b01394

23. G. W. Peterson, J. J. Mahle, J. B. DeCoste, W. O. Gordon, J. A. Rossin, Extraordinary NO_2 removal by the metal-organic framework UiO-66-NH_2. *Angew. Chem. Int. Ed.* **55**, 6235–6238 (2016). doi:10.1002/anie.201601782 Medline

24. P. A. Julien, C. Mottillo, T. Friscic, Metal-organic frameworks meet scalable and sustainable synthesis. *Green Chem.* **19**, 2729–2747 (2017). doi:10.1039/C7GC01078H

25. S. Wang, C. Serre, Toward green production of water-stable metal-organic frameworks based on high-valence metals with low toxicities. *ACS Sustain. Chem.& Eng.* **7**, 11911–11927 (2019). doi:10.1021/acssuschemeng.9b01022

26. M. Bui, C. S. Adjiman, A. Bardow, E. J. Anthony, A. Boston, S. Brown, P. S. Fennell, S. Fuss, A. Galindo, L. A. Hackett, J. P. Hallett, H. J. Herzog, G. Jackson, J. Kemper, S.

Krevor, G. C. Maitland, M. Matuszewski, I. S. Metcalfe, C. Petit, G. Puxty, J. Reimer, D. M. Reiner, E. S. Rubin, S. A. Scott, N. Shah, B. Smit, J. P. M. Trusler, P. Webley, J. Wilcox, N. Mac Dowell, Carbon capture and storage (CCS): The way forward. *Energy Environ. Sci.* **11**, 1062–1176 (2018). doi:10.1039/C7EE02342A

27. R. B. Lin, D. Chen, Y. Y. Lin, J. P. Zhang, X. M. Chen, A zeolite-like zinc triazolate framework with high gas adsorption and separation performance. *Inorg. Chem.* **51**, 9950–9955 (2012). doi:10.1021/ic301463z Medline

28. Y. Y. Lin, Y. B. Zhang, J. P. Zhang, X. M. Chen, Pillaring Zn-triazolate layers with flexible aliphatic dicarboxylates into three-dimensional metal-organic frameworks. *Cryst. Growth Des.* **8**, 3673–3679 (2008). doi:10.1021/cg800289c

29. X.-F. Wei, J. Miao, L.-L. Shi, Synthesis, Crystal Structure, and Luminescent Property of One 3D Porous Metal-Organic Framework With dmc Topology. *Synth. React. Inorg. Met.-Org. Nano-Met. Chem.* **46**, 365–369 (2016). doi:10.1080/15533174.2014.988251

30. S. R. Caskey, A. G. Wong-Foy, A. J. Matzger, Dramatic tuning of carbon dioxide uptake via metal substitution in a coordination polymer with cylindrical pores. *J. Am. Chem. Soc.* **130**, 10870–10871 (2008). doi:10.1021/ja8036096 Medline

31. J. An, S. J. Geib, N. L. Rosi, High and selective CO_2 uptake in a cobalt adeninate metal-organic framework exhibiting pyrimidine- and amino-decorated pores. *J. Am. Chem. Soc.* **132**, 38–39 (2010). doi:10.1021/ja909169x Medline

32. P. Nugent, Y. Belmabkhout, S. D. Burd, A. J. Cairns, R. Luebke, K. Forrest, T. Pham, S. Ma, B. Space, L. Wojtas, M. Eddaoudi, M. J. Zaworotko, Porous materials with optimal adsorption thermodynamics and kinetics for CO_2 separation. *Nature* **495**, 80–84 (2013). doi:10.1038/nature11893 Medline

33. T. M. McDonald, J. A. Mason, X. Kong, E. D. Bloch, D. Gygi, A. Dani, V. Crocellà, F. Giordanino, S. O. Odoh, W. S. Drisdell, B. Vlaisavljevich, A. L. Dzubak, R. Poloni, S. K. Schnell, N. Planas, K. Lee, T. Pascal, L. F. Wan, D. Prendergast, J. B. Neaton, B. Smit, J. B. Kortright, L. Gagliardi, S. Bordiga, J. A. Reimer, J. R. Long, Cooperative insertion of CO_2 in diamine-appended metal-organic frameworks. *Nature* **519**, 303–308 (2015). doi:10.1038/nature14327 Medline

34. P. M. Bhatt, Y. Belmabkhout, A. Cadiau, K. Adil, O. Shekhah, A. Shkurenko, L. J. Barbour, M. Eddaoudi, A Fine-Tuned Fluorinated MOF Addresses the Needs for Trace CO_2 Removal and Air Capture Using Physisorption. *J. Am. Chem. Soc.* **138**, 9301–9307 (2016). doi:10.1021/jacs.6b05345 Medline

35. S. Nandi, S. Collins, D. Chakraborty, D. Banerjee, P. K. Thallapally, T. K. Woo, R. Vaidhyanathan, Ultralow Parasitic Energy for Postcombustion CO_2 Capture Realized in a Nickel Isonicotinate Metal-Organic Framework with Excellent Moisture Stability. *J. Am. Chem. Soc.* **139**, 1734–1737 (2017). doi:10.1021/jacs.6b10455 Medline

36. S. Xiang, Y. He, Z. Zhang, H. Wu, W. Zhou, R. Krishna, B. Chen, Microporous metal-organic framework with potential for carbon dioxide capture at ambient conditions. *Nat. Commun.* **3**, 954 (2012). doi:10.1038/ncomms1956 Medline

37. N. S. Wilkins, J. A. Sawada, A. Rajendran, Measurement of competitive CO_2 and H_2O adsorption on zeolite 13X for post combustion CO_2 capture. *Adsorption* **26**, 765–779 (2020). doi:10.1007/s10450-020-00199-3

38. V. B. López-Cervantes, E. Sánchez-González, T. Jurado-Vázquez, A. Tejeda-Cruz, E. González-Zamora, I. A. Ibarra, CO_2 adsorption under humid conditions: Self-regulated water content in CAU-10. *Polyhedron* **155**, 163–169 (2018). doi:10.1016/j.poly.2018.08.043

39. J. A. Coelho, A. M. Ribeiro, A. F. P. Ferreira, S. M. P. Lucena, A. E. Rodrigues, D. C. S. Azevedo, Stability of an Al-Fumarate MOF and Its Potential for CO_2 Capture from Wet Stream. *Ind. Eng. Chem. Res.* **55**, 2134–2143 (2016). doi:10.1021/acs.iecr.5b03509

40. K. S. Walton, A. R. Millward, D. Dubbeldam, H. Frost, J. J. Low, O. M. Yaghi, R. Q. Snurr, Understanding inflections and steps in carbon dioxide adsorption isotherms in metal-organic frameworks. *J. Am. Chem. Soc.* **130**, 406–407 (2008). doi:10.1021/ja076595g Medline

41. R. Vaidhyanathan, S. S. Iremonger, G. K. H. Shimizu, P. G. Boyd, S. Alavi, T. K. Woo, Direct observation and quantification of CO_2 binding within an amine-functionalized nanoporous solid. *Science* **330**, 650–653 (2010). doi:10.1126/science.1194237 Medline

42. S. Kitagawa, R. Matsuda, Chemistry of coordination space of porous coordination polymers. *Coord. Chem. Rev.* **251**, 2490–2509 (2007). doi:10.1016/j.ccr.2007.07.009

43. M. Jahandar Lashaki, S. Khiavi, A. Sayari, Stability of amine-functionalized CO_2 adsorbents: A multifaceted puzzle. *Chem. Soc. Rev.* **48**, 3320–3405 (2019). doi:10.1039/C8CS00877A Medline

44. P. Hovington, O. Ghaffari-Nik, L. Mariac, A. Liu, B. Henkel, S. Marx, Rapid Cycle Temperature Swing Adsorption Process Using Solid Structured Sorbent for CO_2 capture from Cement Flue Gas, Proceedings of the 15th Greenhouse Gas Control Technologies Conference, 15–18 March 2021.

45. M. Rubio-Martinez, C. Avci-Camur, A. W. Thornton, I. Imaz, D. Maspoch, M. R. Hill, New synthetic routes towards MOF production at scale. *Chem. Soc. Rev.* **46**, 3453–3480 (2017). doi:10.1039/C7CS00109F Medline

46. J. M. Taylor, R. K. Mah, G. K. H. Shimizu, Synthesis of Zinc MOF Materials, PCT/CA2019/050530, filed 24 April 2019.

47. S. N. Bizzari, M. Blagoev, CEH Marketing Research Report, *Chemical Economics Handbook*, SRI Consulting, April 2010.

48. A. U. Czaja, N. Trukhan, U. Müller, Industrial applications of metal-organic frameworks. *Chem. Soc. Rev.* **38**, 1284–1293 (2009). doi:10.1039/b804680h Medline

49. A. K. Rajagopalan, A. M. Avila, A. Rajendran, Do adsorbent screening metrics predict process performance? A process optimisation based study for post-combustion capture of CO_2. *Int. J. Greenh. Gas Control* **46**, 76–85 (2016). doi:10.1016/j.ijggc.2015.12.033

50. J. Park, H. O. Rubiera Landa, Y. Kawajiri, M. J. Realff, R. P. Lively, D. S. Sholl, How Well Do Approximate Models of Adsorption-Based CO_2 Capture Processes Predict Results of

Detailed Process Models? *Ind. Eng. Chem. Res.* **59**, 7097–7108 (2020). doi:10.1021/acs.iecr.9b05363

51. K. T. Leperi, Y. G. Chung, F. You, R. Q. Snurr, Development of a General Evaluation Metric for Rapid Screening of Adsorbent Materials for Postcombustion CO_2 Capture. *ACS Sustain. Chem.& Eng.* **7**, 11529–11539 (2019). doi:10.1021/acssuschemeng.9b01418

52. M. Khurana, S. Farooq, Adsorbent Screening for Postcombustion CO_2 Capture: A Method Relating Equilibrium Isotherm Characteristics to an Optimum Vacuum Swing Adsorption Process Performance. *Ind. Eng. Chem. Res.* **55**, 2447–2460 (2016). doi:10.1021/acs.iecr.5b04531

53. A. H. Farmahini, S. Krishnamurthy, D. Friedrich, S. Brandani, L. Sarkisov, Performance-Based Screening of Porous Materials for Carbon Capture. *Chem. Rev.* **121**, 10666–10741 (2021). doi:10.1021/acs.chemrev.0c01266 Medline

54. T. D. Burns, K. N. Pai, S. G. Subraveti, S. P. Collins, M. Krykunov, A. Rajendran, T. K. Woo, Prediction of MOF performance in vacuum swing adsorption systems for postcombustion CO_2 capture based on integrated molecular simulations, process optimizations, and machine learning models. *Environ. Sci. Technol.* **54**, 4536–4544 (2020). doi:10.1021/acs.est.9b07407 Medline

55. A. Samanta, A. Zhao, G. K. H. Shimizu, P. Sarkar, R. Gupta, Post-Combustion CO_2 Capture Using Solid Sorbents: A Review. *Ind. Eng. Chem. Res.* **51**, 1438–1463 (2012). doi:10.1021/ie200686q

56. R. L. Siegelman, E. J. Kim, J. R. Long, Porous materials for carbon dioxide separations. *Nat. Mater.* **20**, 1060–1072 (2021). doi:10.1038/s41563-021-01054-8 Medline

57. O. V. Dolomanov, L. J. Bourhis, R. J. Gildea, J. A. K. Howard, H. Puschmann, J. A. K., Howard, H. Puschmann, *OLEX2*: A complete structure solution, refinement and analysis program. *J. Appl. Cryst.* **42**, 339–341 (2009). doi:10.1107/S0021889808042726

58. G. M. Sheldrick, A short history of SHELX. *Acta Crystallogr. A* **64**, 112–122 (2008). doi:10.1107/S0108767307043930 Medline

59. G. M. Sheldrick, Crystal structure refinement with SHELXL. *Acta Crystallogr. C Struct. Chem.* **71**, 3–8 (2015). doi:10.1107/S2053229614024218 Medline

60. P. Goyal, M. J. Purdue, S. Farooq, Adsorption and diffusion of moisture and wet flue gas on silica gel. *Chem. Eng. Sci.* **227**, 115890 (2020). doi:10.1016/j.ces.2020.115890

61. N. S. Wilkins, A. Rajendran, S. Farooq, Dynamic column breakthrough experiments for measurement of adsorption equilibrium and kinetics. *Adsorption* **27**, 397–422 (2021). doi:10.1007/s10450-020-00269-6

62. A. K. Rappe, C. J. Casewit, K. S. Colwell, W. A. Goddard III, W. M. Skiff, UFF, a full periodic table force field for molecular mechanics and molecular dynamics simulations. *J. Am. Chem. Soc.* **114**, 10024–10035 (1992). doi:10.1021/ja00051a040

63. A. García-Sánchez, C. O. Ania, J. B. Parra, D. Dubbeldam, T. J. H. Vlugt, R. Krishna, S. Calero, Transferable Force Field for Carbon Dioxide Adsorption in Zeolites. *PhysChemComm* **113**, 8814–8820 (2009).

64. B. Provost, “An Improved N_2 Model for Predicting Gas Adsorption in MOFs and using Molecular Simulation to aid in the Interpretation of SSNMR Spectra of MOFs,” thesis, University of Ottawa (2015).

65. H. W. Horn, W. C. Swope, J. W. Pitera, J. D. Madura, T. J. Dick, G. L. Hura, T. Head-Gordon, Development of an improved four-site water model for biomolecular simulations: TIP4P-Ew. *J. Chem. Phys.* **120**, 9665–9678 (2004). doi:10.1063/1.1683075 Medline

66. M. Zein Aghaji, “Large Scale Computational Screening of Metal Organic Framework Materials for Natural Gas Purification,” thesis, University of Ottawa (2017).

67. C. Campañá, B. Mussard, T. K. Woo, Electrostatic Potential Derived Atomic Charges for Periodic Systems Using a Modified Error Functional. *J. Chem. Theory Comput.* **5**, 2866–2878 (2009). doi:10.1021/ct9003405 Medline

68. G. Kresse, J. Hafner, Ab initio molecular dynamics for liquid metals. *Phys. Rev. B Condens. Matter* **47**, 558–561 (1993). doi:10.1103/PhysRevB.47.558 Medline

69. G. Kresse, J. Furthmüller, Efficiency of ab-initio total energy calculations for metals and semiconductors using a plane-wave basis set. *Comput. Mater. Sci.* **6**, 15–50 (1996). doi:10.1016/0927-0256(96)00008-0

70. G. Kresse, J. Furthmüller, Efficient iterative schemes for ab initio total-energy calculations using a plane-wave basis set. *Phys. Rev. B Condens. Matter* **54**, 11169–11186 (1996). doi:10.1103/PhysRevB.54.11169 Medline

71. J. P. Perdew, K. Burke, M. Ernzerhof, Generalized gradient approximation made simple. *Phys. Rev. Lett.* **77**, 3865–3868 (1996). doi:10.1103/PhysRevLett.77.3865 Medline

72. G. Kresse, D. Joubert, From ultrasoft pseudopotentials to the projector augmented-wave method. *Phys. Rev. B Condens. Matter* **59**, 1758–1775 (1999). doi:10.1103/PhysRevB.59.1758

73. I. T. Todorov, W. Smith, K. Trachenko, M T. Dove, DL_POLY_3: New dimensions in molecular dynamics simulations via massive parallelism. *J. Mater. Chem.* **16**, 1911–1918 (2006). doi:10.1039/b517931a

74. P. Virtanen, R. Gommers, T. E. Oliphant, M. Haberland, T. Reddy, D. Cournapeau, E. Burovski, P. Peterson, W. Weckesser, J. Bright, S. J. van der Walt, M. Brett, J. Wilson, K. J. Millman, N. Mayorov, A. R. J. Nelson, E. Jones, R. Kern, E. Larson, C. J. Carey, İ. Polat, Y. Feng, E. W. Moore, J. VanderPlas, D. Laxalde, J. Perktold, R. Cimrman, I. Henriksen, E. A. Quintero, C. R. Harris, A. M. Archibald, A. H. Ribeiro, F. Pedregosa, P. van Mulbregt, A. Vijaykumar, A. P. Bardelli, A. Rothberg, A. Hilboll, A. Kloeckner, A. Scopatz, A. Lee, A. Rokem, C. N. Woods, C. Fulton, C. Masson, C. Häggström, C. Fitzgerald, D. A. Nicholson, D. R. Hagen, D. V. Pasechnik, E. Olivetti, E. Martin, E. Wieser, F. Silva, F. Lenders, F. Wilhelm, G. Young, G. A. Price, G.-L. Ingold, G. E. Allen, G. R. Lee, H. Audren, I. Probst, J. P. Dietrich, J. Silterra, J. T. Webber, J. Slavič, J. Nothman, J. Buchner, J. Kulick, J. L. Schönberger, J. V. de Miranda Cardoso, J. Reimer, J. Harrington, J. L. C. Rodríguez, J. Nunez-Iglesias, J. Kuczynski, K. Tritz, M. Thoma, M. Newville, M. Kümmerer, M. Bolingbroke, M. Tartre, M. Pak, N. J. Smith, N. Nowaczyk, N. Shebanov, O. Pavlyk, P. A. Brodtkorb, P. Lee, R. T. McGibbon, R. Feldbauer, S. Lewis, S. Tygier, S. Sievert, S. Vigna, S. Peterson, S. More, T. Pudlik, T. Oshima, T. J. Pingel, T. P. Robitaille, T. Spura, T. R. Jones, T. Cera, T. Leslie, T. Zito, T. Krauss, U. Upadhyay, Y. O. Halchenko, Y. Vázquez-Baeza; SciPy 1.0 Contributors, SciPy 1.0: Fundamental algorithms for scientific computing in Python. *Nat. Methods* **17**, 261–272 (2020). doi:10.1038/s41592-019-0686-2 Medline